Identification of the process windows of inclined rotating fixed-bed reactors with concentric tube – a hydrodynamic analysis

Timaeus, R.; Schleicher, E.; Bieberle, A.; Hampel, U.; Schubert, M.;

Originally published:

July 2020

Chemical Engineering Science 220(2020), 115637

DOI: https://doi.org/10.1016/j.ces.2020.115637

Perma-Link to Publication Repository of HZDR:

https://www.hzdr.de/publications/Publ-30121

Identification of the process windows of inclined rotating fixed-bed reactors with concentric tube – a hydrodynamic analysis

Robert Timaeus[a,*], *Eckhard Schleicher*[a], *André Bieberle*[a], *Uwe Hampel*[a,b], *Markus Schubert*[a,*]

[a] Helmholtz-*Zentrum Dresden-Rossendorf, Bautzner Landstraße 400, 01328 Dresden, Germany.*

[b] *TU Dresden, Institute of Power Engineering, 01069 Dresden, Germany.*

** Corresponding authors: r.timaeus@hzdr.de, m.schubert@hzdr.de*

Abstract: The inclined rotating fixed-bed reactor with inner tube is a promising process intensification concept for gas-limited reactions. In order to take full advantage of the reactor concept the installation of an inner concentric displacement tube is proposed to support the wetting intermittency of the whole fixed-bed at different liquid filling levels. The effects of operating conditions and design parameters on flow stratification, liquid filling level and specific pressure drop are analysed to identify the process window. In particular, the influence of superficial phase velocities, inclination angle, rotational velocity, particle diameter and inner tube diameter are studied. The liquid phase distribution is characterized with a capacitance-based wire-mesh sensor, which is adapted to cope with organic liquid, porous alumina catalyst packings and reactor rotation. Furthermore, the radial porosity distribution in the annular fixed-beds is determined using gamma-ray computed tomography.

Keywords: Inclined rotating fixed-bed, Process intensification, Capacitance wire-mesh sensor, Multiphase reactor

1 Introduction

The performance of multiphase reactors is often limited by mass transfer processes (Utikar and Ranade, 2017). Especially, trickle-bed reactors (TBR) are frequently used

for reactions with fast kinetics, which are controlled by the gas transfer (Mills and Duducović´, 1980). Here, the liquid film on the solid catalysts acts as mass transfer barrier (Boelhouwer et al., 2002a). Several reactor concepts and operation strategies have been proposed to intensify the mass transfer (Nigam and Larachi, 2005).

Structured reactors with novel packings were suggested to intensify the gas-liquid-solid contact. For example, Taylor flow in monolith reactors was found to feature low pressure drop, high specific surface area and improved catalyst wetting (Haase et al., 2016). For example, Nijhuis et al. (2001) obtained higher productivities for α-methylstyrene and benzaldehyde hydrogenations in a pilot-scale monolith reactor compared to a conventional trickle-bed reactor. Open-cell solid foams are another promising replacement for conventional fixed-bed reactors with randomly packed beds. Here, the solid material network provides high void space and specific surface area, while the pressure drop is low (Edouard et al., 2008; Zalucky et al., 2017a). The skeletal structure of the solid foams leads also to a higher thermal conductivity enhancing the radial heat transfer (Wallenstein et al., 2014), which is especially beneficial for exothermic reactions. Applying the limiting current technique, Zalucky et al. (2017b) confirmed also higher liquid-solid mass transfer coefficients in solid foams.

Recently, Gelhausen et al. (Gelhausen et al., 2017) proposed a siphon reactor to increase gas-solid and gas-liquid mass transfer. Here, the catalyst is alternatingly exposed to gas and liquid based on a customized self-sustaining liquid filling-draining cycle in packing segments. Beyond the adjustable gas-solid or liquid-solid contact time, stagnant liquid is effectively discharged at each cycle. Compared to a conventional TBR, a twofold increase of the space-time yield (STY) was obtained for the hydrogenation of 2-butyne-1,4-diol.

Periodic operation of TBRs was proposed as a process intensification method (Lange et al., 1994; Castellari and Haure, 1995). Here, the liquid flow rate is cycled at the reactor inlet to induce a temporal modulation of the liquid holdup along the fixed-bed in order to decrease the liquid film thickness surrounding the catalyst. This way, the access of gaseous educts to the catalysts at low local liquid holdups is facilitated. Many lab-scale studies confirmed significantly increasing STY via flow modulation (Banchero et al., 2004; Khadlikar et al., 1999). However, such induced liquid pulses

rapidly decay along the fixed-bed (Boelhouwer et al., 2002b), which eliminates beneficial conditions at lower reactor positions (Dietrich et al., 2005).

Thus, Härting et al. (2015) introduced the inclined rotating fixed-bed reactor (IRR) concept, where the superposition of reactor inclination and rotation at moderate rotational velocities shape a stratified flow. Such flow pattern yields a spatial modulation of the liquid holdup along the whole fixed bed. The process intensification potential was studied for α-methylstyrene hydrogenation and returned almost doubled conversion rates compared to the conventional TBR.

However, a stratified flow, which ensures a binary wetting cycle of the whole catalyst bed, i.e. ideal flow stratification with liquid filling level of exactly 50%, can hardly be adjusted. To enlarge the beneficial process window towards lower liquid holdups and to adjust the respective durations of the wetting and draining parts, Schubert (2018) proposed an advanced IRR design with a concentric inner tube (Figure 1a).

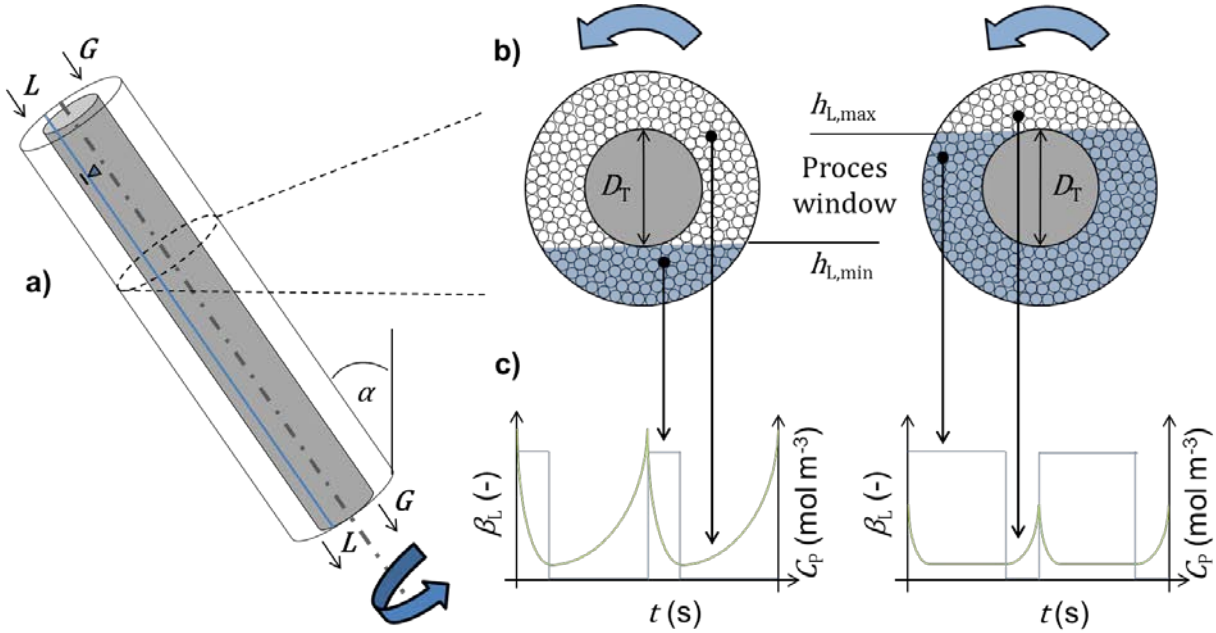

Figure 1: a) IRR concept with concentric inner tube and (b) minimum and maximum liquid filling level h_L, in the cross-section of the IRR indicating the beneficial process window with (c) corresponding local liquid saturation β_L and product concentration at the catalyst surface C_P.

This advanced reactor design enables full utilization of the catalyst as long as the liquid filling level h_L is between lower and upper heights ($h_{L,min} \leq h_L \leq h_{L,max}$) of the

inner tube (Figure 1b). Accordingly, inner tube diameter and reactor diameter are crucial geometric parameters of this advanced reactor concept. A recent numerical analysis for the α-methylstyrene hydrogenation based on a heterogeneous continuum model revealed the potential of the advanced design (Timaeus et al., 2019a). Compared to the previous concept of Härting et al. (2015), a further increase of the STY was obtained at lower gas-liquid interface positions (Figure 1b, left). Here, the catalyst particles experience the wetting intermittency with a longer period at drained conditions, which intensifies the gas mass transfer to the catalysts even more (Figure 1c, left).

The objective of this work is to identify the process windows for the stratified flow in the IRR with concentric inner tube to fully utilize the potential of that reactor concept. In particular, flow pattern, liquid filling level, and specific pressure drop are analysed depending on superficial phase velocities, inclination angle, rotational velocity, particle diameter and inner tube diameter. For the flow visualization, capacitance-based wire-mesh sensors (WMSs) are applied to distinguish liquid (cumene) and gas (nitrogen) in the fixed-bed (porous alumina particles) based on the relative permittivities (Timaeus et al., 2019b).

2 Material and methods

2.1 Experimental setup

The experimental setup of the IRR (1) with concentric inner tube (2) is schematically shown in Figure 2. Reactor and concentric inner tube of the IRR are made of three stainless steel segments. The upper and lower segments have a length of 0.3 m, while the middle segments have a length of 1.0 m. The inner reactor diameter D_0 is 0.1 m and the interchangeable inner tubes have outer diameters D_Γ of 0.03 m or 0.05 m. The resulting annular gaps of 25 mm or 35 mm, respectively, are filled with porous alumina particles of 2.5 mm or 4.5 mm mean diameter. To prevent both particle motion relative to the IRR rotation and particle abrasion, two grids installed at reactor inlet and outlet immobilize the particle packing in between. Three configurations of the IRR are installed, which are defined by concentric tube diameter and particle diameter as summarized in Table 1.

Table 1: Configurations of the IRR with inner tube and corresponding dimensions.

Configuration	Tube diameter (mm)	Particle diameter (mm)	Gap-to-particle-diameter ratio
A	50	4.5	5.5
B	50	2.5	10
C	30	4.5	7.8

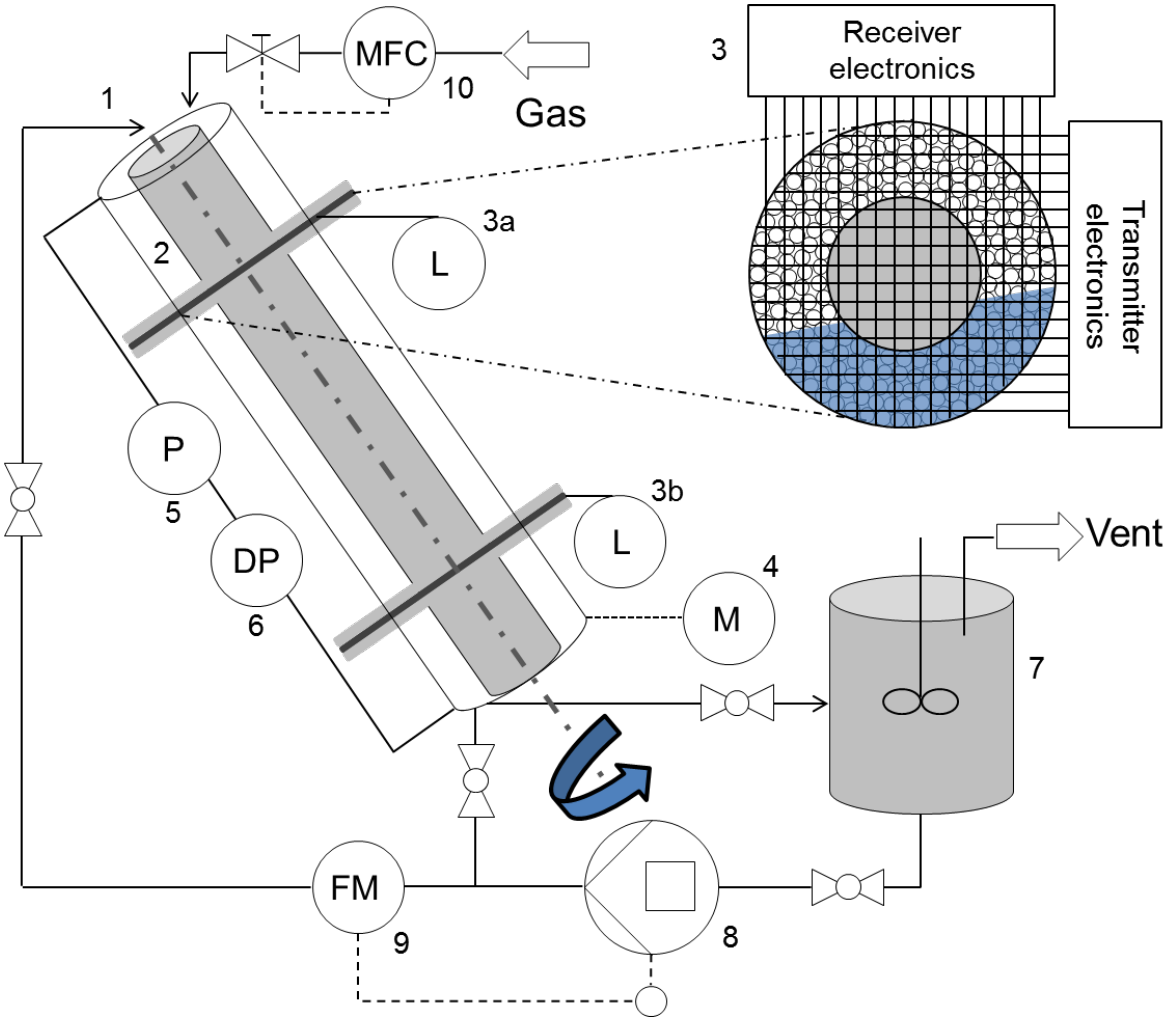

Figure 2: Inclined rotating fixed-bed reactor setup with capacitance wire-mesh sensors (1 – reactor, 2 – inner tube, 3a,b – capacitance wire-mesh sensors with autarkic sensor electronics, 4 – hollow shaft rotary actuator, 5 – absolute pressure transducer, 6 – difference pressure transducer, 7 – gas-liquid separator, 8 – lobe rotor pump, 9 – Coriolis liquid flow meter, 10 – gas mass flow controller).

The reactor is installed in an inclinable rack and can be adjusted at arbitrary inclination angles from horizontal to vertical orientation. The capacitance WMSs (3) are flange-mounted between the reactor segments. A hollow shaft rotary actuator (4, DG130R-ASAC, Oriental Motor) with a stepper motor is used to rotate the IRR. To cope with the rotating reactor, wireless power supply and data acquisition are utilized. Two power banks are mounted on the reactor to operate the WMSs as well as absolute (5, PAA23SY, Omega) and differential (6, PD23, Omega) pressure transducers. Moreover, a WLAN module is fixed at the IRR to connect the sensors to a measurement computer for the data acquisition. The liquid mass flow is adjusted via lobe rotor pump (8, MDL0230, Waukesha Cherry-Burrell) controlled by a Coriolis liquid flow meter (9, Optimass 1300C, Krohne) and the gas flow rate is controlled via mass flow controller (10, FMA-2611A, Omega). It should be noted that the superficial velocities provided below refer to the cross-sectional area of the annuli available for the flow. Gas (nitrogen) and liquid (cumene, purity of 99.9 %, Acros Organics) are co-currently introduced at top of the IRR and a gas-liquid separator is installed downstream the IRR (7). Here, gas is released to the in-house ventilation system and liquid is recycled. The measurements were conducted at ambient pressure and room temperature.

2.2 Capacitance wire-mesh sensors

Low-intrusive capacitance WMSs are used to visualize the flow and to determine the liquid filling level h_L in the IRR. Each WMS consists of 16 receiver and 16 transmitter wires orthogonally arranged with a small axial offset of 2.5 mm. 176 out of the 256 wire crossing points are located within in the cross-section of the annulus. Their spatial separation is 6.25 mm. The sensor data are read out with a temporal resolution of 25 Hz, which is sufficient for the evolving quasi-stationary flows in the IRR. Naturally, same liquid distributions are obtained at both sensor positions, thus, only data of the lower WMS, i.e. 0.3 m upstream the reactor outlet, are processed and discussed below. It should be noted that the second WMS could be used in the future for transient tracer studies to reveal the liquid residence time and dispersion behavior. Liquid absorbed in the pore network of the catalyst particles and static liquid trapped between catalyst particles cannot be distinguished from the flowing liquid by the WMS. Hence, the obtained local liquid fractions β_L are considered as so-

called reduced liquid saturations, i.e. dynamic liquid fractions related to the interstitial void space of the fixed-bed reduced by the static liquid. The allocation of involved phases in the IRR to certain fractions is exemplarily shown in Figure 3.

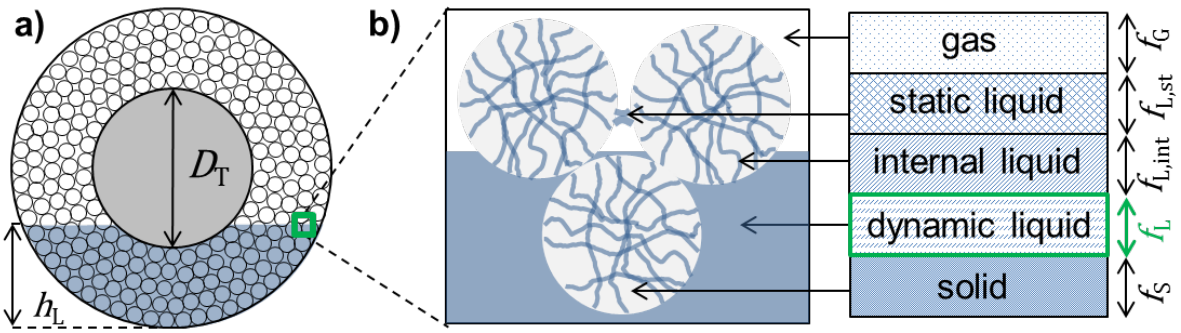

Figure 3: a) Phase distribution in the cross-section of the IRR with marked liquid filling level h_L and b) allocation of occurring phases in the IRR to certain fractions, which are: gas: continuous gas phase of the stratified flow pattern, static liquid: external liquid trapped between the catalyst, internal liquid: liquid inside the catalyst pores, dynamic liquid: external flowing liquid, solid: skeletal aluminum structure of the catalyst.

The measuring principle of the capacitance WMS is based on the logarithmic relation between the output voltage V_0 of the transimpedance amplifier of the WMS and the permittivity of a sensing point according to

$$V_{\log} = a \cdot \ln(\varepsilon_X + \varepsilon_P) + b, \tag{1}$$

where, a and b are geometry-related constants, ε_X and ε_P are the permittivities accounting for fluid phases and solid packing, respectively. Recently, it was shown that the permittivity ε_P of a constant solid fraction can be neglected as the deviation is less than 2% for the cross-sectionally averaged β_L at stratified flow (Timaeus et al., 2019b). Thus, the unknown constants a and b can be obtained via two reference scans (flooded and drained fixed-bed). Accordingly, a linear dependence between β_L and the measured permittivity ε_{Meas} is assumed (Bierberle et al., 2010; Prasser et al., 1998; da Silva et al., 2007) and β_L can be determined as

$$\beta_{\mathrm{L}} = \frac{\varepsilon_{\mathrm{Meas}} - \varepsilon_{\mathrm{G}}}{\varepsilon_{\mathrm{L}} - \varepsilon_{\mathrm{G}}}, \tag{2}$$

where ε_{L} and ε_{G} are the permittivies of gas and liquid phases, respectively. This way, β_{L} is calculated for each crossing point exposed to the flow. Subsequently, average liquid saturation and corresponding liquid filling level h_{L} are determined from 7500 frames obtained for a measurement duration of 300 seconds with a frequency of 25 Hz. Further details of the capacitance WMS and the data processing are summarized in Timaeus et al. (2019b).

2.3 Porosity of the annular packed bed

The porosity of the annular packed bed near the walls can significantly deviate from the bulk porosity (Sodré and Parise, 1998; du Toit, 2008). Accordingly, higher interstitial phase velocities near the walls affect mass transfer and residence time behavior of the IRR. Cheng and Hsu (Cheng and Hsu, 1986) proposed an exponential approximation of the porosity in an annulus packed with spheres according to

$$\varepsilon(r) = \begin{cases} \varepsilon_{\mathrm{b}}\left(1 + C\exp\left(-N\dfrac{r - R_{\mathrm{T}}}{d_{\mathrm{P}}}\right)\right) & \text{for } R_{\mathrm{T}} \le r \le \dfrac{R_{\mathrm{T}} + R_{\mathrm{O}}}{2}, \\ \varepsilon_{\mathrm{b}}\left(1 + C\exp\left(-N\dfrac{R_{\mathrm{O}} - r}{d_{\mathrm{P}}}\right)\right) & \text{for } \dfrac{R_{\mathrm{T}} + R_{\mathrm{O}}}{2} \le r \le R_{\mathrm{O}}, \end{cases} \tag{3}$$

where r is the radial coordinate, R_{T} is the inner tube radius, R_{O} is the reactor radius, ε_{b} is the bulk porosity of the packed bed and C and N are fitting parameters. According to (Vortmeyer and Schuster, 1983; Cheng and Hsu, 1986; Hunt and Tien, 1990), C is used to fulfill

$$\varepsilon(r = R_{\mathrm{T}}) = \varepsilon(r = R_{\mathrm{O}}) = 1. \tag{4}$$

Furthermore, N describes the slope of the porosity in the vicinity of the walls and a wide range for N is reported in the literature (du Toit, 2008; Vortmeyer and Schuster, 1983; Cheng and Hsu 1986). For example, Cheng and Hsu (1986) applied N = 2, while Hunt and Tien (1988) proposed N = 8. Sodre and Parise (1998) described a

linear relation between particle-to-annulus diameter ratio and N, however, non-linear behavior is rather expected at wider parameter range. Thus, N for the IRR is derived from the porosity profile obtained via gamma-ray computed tomography (CT) with a collimated ^{137}Cs source (662 keV gamma-photon energy). Details about the non-invasive gamma-ray imaging and corresponding data processing can be found at Bieberle et al. (2010). The tomographic experiments were conducted with annular packed beds of 0.3 m length for the configurations listed in Table 1 (see Section 2.1). Exemplarily, the cross-sectional distribution of the normalized attenuation coefficients A_{CT} of Configuration A is shown in Figure 4a.

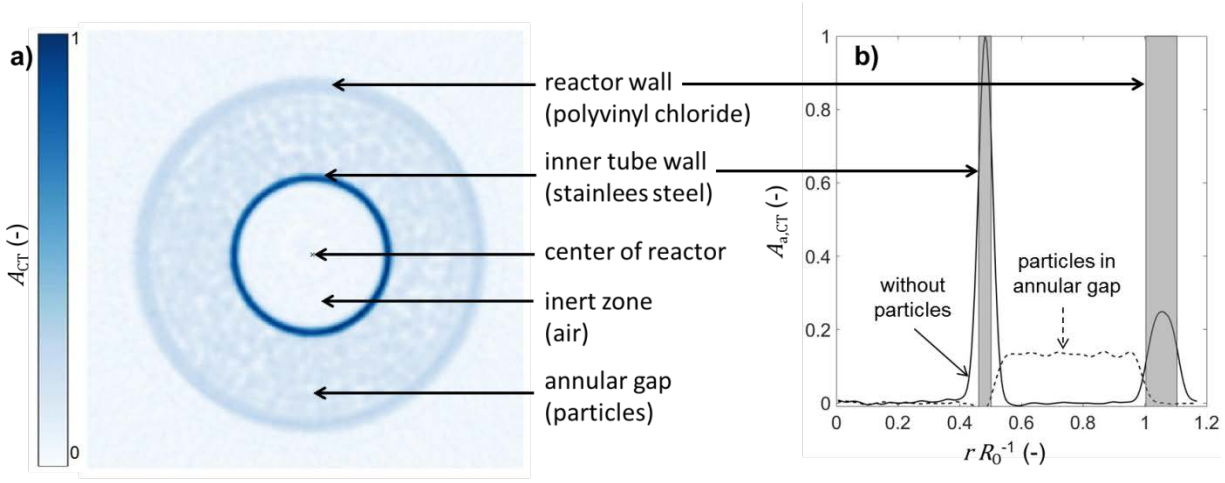

Figure 4: a) Cross-sectional distribution of the normalized attenuation coefficients A_{CT} of the IRR (Configuration A) and b) corresponding radial profiles of the azimuthally averaged $A_{\mathrm{a,CT}}$ with and without packed bed (the latter profile is utilized to locate the position of the packed bed).

Additionally, measurements without particles were carried out to detect the exact positions of the annuli. Here, the local maxima define the centers of the inner and outer tube walls. The radial profiles of the two associated normalized attenuation-coefficients $A_{\mathrm{a,CT}}$ for Configuration A are shown in Figure 4b. To assign densities to the attenuation coefficients, the total weight of the packing was considered and a least square optimization was performed according to

$$\min_{\rho}\left(\iiint A_{\mathrm{a,CT}}(r)\rho r\mathrm{d}r\mathrm{d}\varphi\mathrm{d}z - m_{\mathrm{bed}}\right)^2, \tag{5}$$

where, ρ is the fitted density and m_{bed} is the mass of the annular packed bed. The porosity of the packed bed is defined as

$$\varepsilon(r) = \frac{\rho_{\mathrm{P}} - \rho_{\mathrm{bed}}(r)}{\rho_{\mathrm{P}} - \rho_{\mathrm{G}}}, \tag{6}$$

where ρ_{P}, ρ_{bed} and ρ_{G} are the densities of particles, packed bed and gaseous phase. Eventually, the bulk porosity ε_{b} is obtained from the radial porosity profile, which enables the determination of the parameter N by a least square fit. In Figure 5a the porosity distribution of Configuration A obtained by the procedure described above is exemplarily shown.

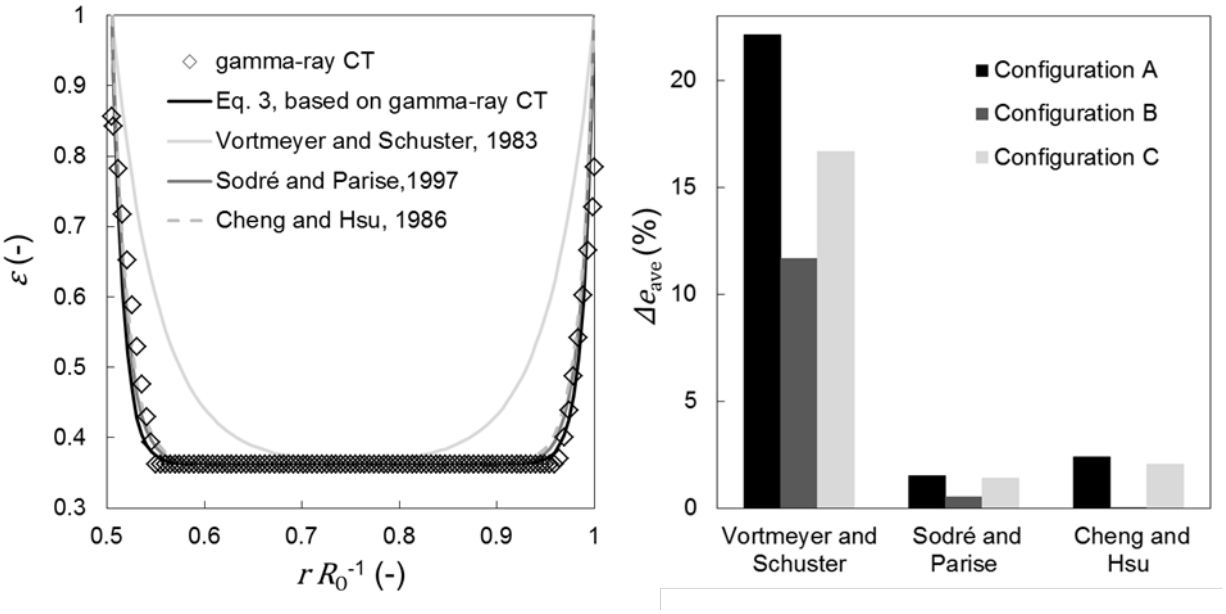

Figure 5: a) Porosity profile of Configuration A (D_{T} = 5 cm, d_{P} = 4.5 mm) obtained tomographically and predicted with Eq. 3 for various N proposed in the literature and b) deviations between measured and predicted average porosities.

Additionally, predictions for the porosity profiles using Eq. 2 are shown for N fitted to the experimental data and proposed in the literature. Figure 5b shows the deviations Δe between the various predictions for the average porosity and the experimental value. The determined parameters for each configuration of the IRR are summarized in Table 2. The shown attenuation coefficients and the porosity data are available in RODARE: 10.14278/rodare.204 [dataset] (Timaeus et al., 2019).

Table 2: Porosity data and determined parameters of the exponential approximations based on gamma-ray CT scans.

Configuration	ε_{ave} (m_V^3 m_R^{-3})	ε_b (m_V^3 m_R^{-3})	C (-)	N (-)
A	0.392	0.362	1.76	8.02
B	0.375	0.352	1.84	5.99
C	0.380	0.359	1.78	8.37

3 Results

The hydrodynamic characterization of the new IRR design comprises phase distribution, liquid filling level and specific pressure drop. The operating conditions are chosen to adjust the stratified flow, ensuring the beneficial wetting intermittency. Here, low to moderate rotational velocities are of particular interest as observed by Härting et al. in reaction studies with the first generation design of the IRR (Härting et al., 2015). Initially, the cross-sectional phase distribution in the IRR is visualized for each operating point to identify the flow regime using the WMS sensor 3b. Figure 6 summarizes the patterns for different rotational velocities and inclination angles for Configuration A.

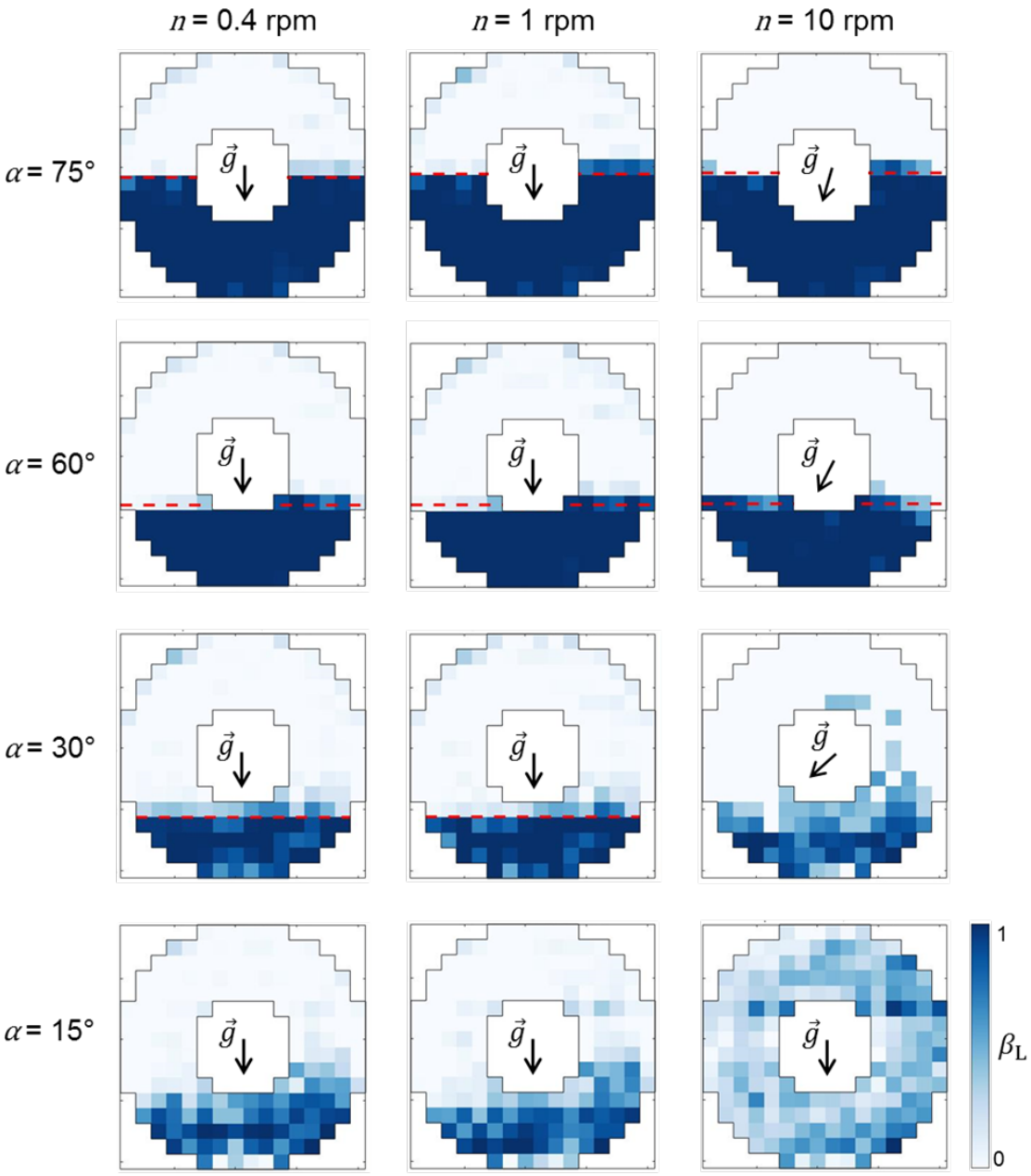

Figure 6: Cross-sectional saturation distribution for Configuration A (D_T = 5 cm, d_P = 4.5 mm) at u_L = 0.01 m s^{-1}, u_G = 0.05 m s^{-1} and different rotational velocities n and inclination angles α. Gravity vector $\vec{g}$ and gas-liquid interface of the stratified flow patterns (dashed line) are also shown.

The liquid filling level h_L, i.e. height of the gas-liquid interface position for the stratified flow patterns, is determined according to the procedure explained in Section 2.2 (highlighted with a horizontal dashed red line). The gravity vector indicates the bottommost position of the reactor cross-section.

At low inclination angles (α = 15° and 30°) and high rotational velocities (n = 10 rpm) the flow stratification vanishes. Here, the effects of the centrifugal force excel the gravitational force counterparts and the operating conditions result in liquid filling levels, which are beyond the beneficial IRR process window. Below, the effects of superficial phase velocities, inclination angle, rotational velocity, particle size and inner tube diameter on normalized liquid filling level ($H_L = h_L / D_O$) and specific pressure drop are discussed in detail.

3.1 Effects of superficial liquid velocity and inclination angle

Figure 7a shows H_L as function of the superficial liquid velocity u_L for inclination angles between 15° to 75° at a rotational velocity of 1 rpm for a superficial gas velocity of 0.05 m s^{-1}. The beneficial hydrodynamic process window is defined by inner tube and reactor diameters (D_T and D_O), which set minimum and maximum normalized liquid filling levels ($H_{L,min}$ and $H_{L,max}$), enabling a wetting intermittency for the whole fixed-bed. For Configurations A and B, $H_{L,min}$ and $H_{L,max}$ are 0.25 and 0.75, respectively (indicated by the shaded area in Figure 7a). Additionally, the corresponding specific pressure drop $\Delta p\, L^{-1}$ is shown in Figure 7b.

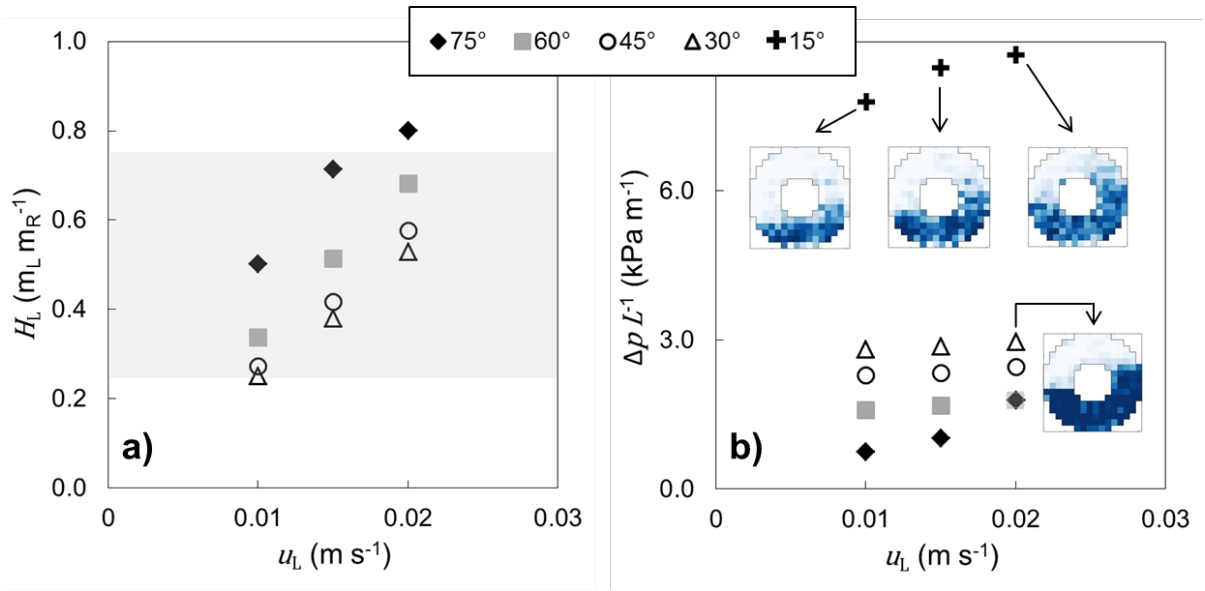

Figure 7: a) Normalized liquid filling level H_L and (b) specific pressure drop $\Delta p\, L^{-1}$ depending on superficial liquid velocity u_L and inclination angle α (n = 1 rpm, u_G = 0.05 m s^{-1}, D_T = 5 cm, d_P = 4.5 mm). The shaded area indicates the

hydrodynamic process window for the IRR (same notation is used in the figures below).

Logically, H_L increases with increasing superficial liquid velocity regardless of the inclination angle. The same trend is obtained for the specific pressure drop. Here, higher solid-fluid phase interactions occur at higher superficial liquid velocities due to less accessible cross-section per fluid phase. Considering the stratified flow patterns, the specific pressure drop is most sensitive to the liquid load at inclination angles of 75°, where H_L reaches the highest values.

H_L also increases with increasing inclination angle due to the lower downhill driving force. This increases the residence time of the liquid. The effect of the inclination angle on H_L decreases with lower inclination angles. Contrary, the specific pressure drop decreases with increasing inclination angles. Here, the gas-liquid interactions reduce with more pronounced phase stratification. In particular, a strong increase of the specific pressure drop occurs from 30° to 15°, which can be explained by the transition from stratified to sickle flow as illustrated in Figure 7b.

For the highest superficial liquid velocity of 0.02 m s^{-1} at an inclination angle of 75° H_L exceeds the inner tube. Thus, parts of the catalyst packing are excluded from the advantageous wetting intermittency and rotate permanently within the liquid phase without access to the gas phase.

The results reveal that the selection of inclination angle and superficial liquid velocity enables an arbitrary adjustment of the gas-liquid interface position to tune the duration of the catalyst immersion per reactor rotation, also referred to as ‘split’ in periodically operated trickle-bed reactors. From a reaction engineering point of view, H_L can be adjusted to $H_{L,min}$ to increase the gas-solid mass transfer for reaction systems with excess of liquid educt. At the same time, the residence time of the liquid phase is decreased, which leads to a trade-off between high residence time and beneficial mass transfer conditions. Contrary, if liquid educt depletion occurs H_L can be increased accordingly.

3.2 Effect of rotational velocity

The immersion and draining durations of the catalysts are adjusted by the rotational velocity. Here, a range between 0.4 rpm and 10 rpm was investigated. Figure 8 shows H_L and $\Delta p\ L^{-1}$ as a function of the rotational velocity at superficial liquid and gas velocity of 0.01 m s^{-1} 0.05 m s^{-1}, respectively, for Configuration A.

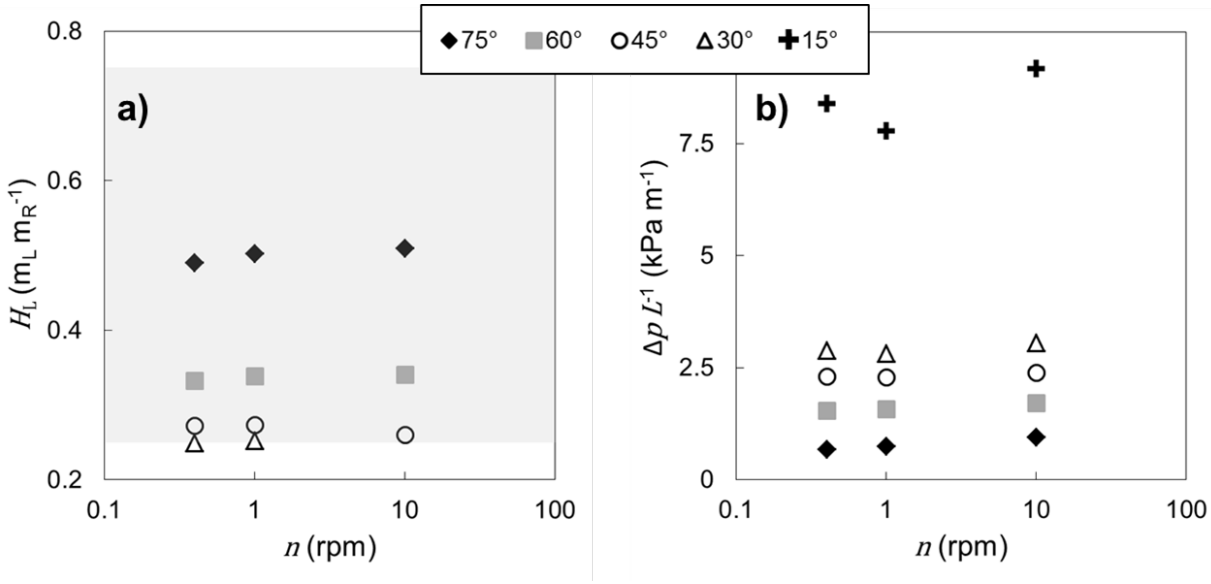

Figure 8: Effect of the rotational velocity on a) liquid filling level H_L (only data for stratified flow are shown) and b) specific pressure drop $\Delta p\ L^{-1}$ for different inclination angles (u_G = 0.05 m s^{-1}, u_L = 0.01 m s^{-1}, D_T = 5 cm, d_P = 4.5 mm).

H_L slightly increases with increasing rotational velocity as a consequence of higher liquid residence time at higher rotational velocities. Here, increasing transversal forces act against the bulk flow. However, the effect of the rotational velocity is low compared to the effects of inclination angle and superficial liquid velocity.

The same trend is observed for the specific pressure drop as long as stratified flow is present. The transition from stratified to dispersed flow at an inclination angle of 15° results in a large increase of the specific pressure drop due to significantly higher interactions between the fluid phases.

At a rotational velocity of 0.4 rpm and an inclination angle of 30° H_L is below the inner tube, thus, parts of the catalyst packing are excluded from the wetting intermittency

and rotate permanently within the gas phase without access to the liquid bulk phase. Such operating conditions cause severe liquid educt depletion.

3.3 Effect of superficial gas velocity

The superficial gas velocity is crucial for the gas-solid mass transfer in the drained sections of the catalyst packings. In Figure 9, H_L and $\Delta p\, L^{-1}$ are shown as a function of the superficial gas velocity ranging from 0.05 m s^{-1} to 0.15 m s^{-1}, for Configuration A.

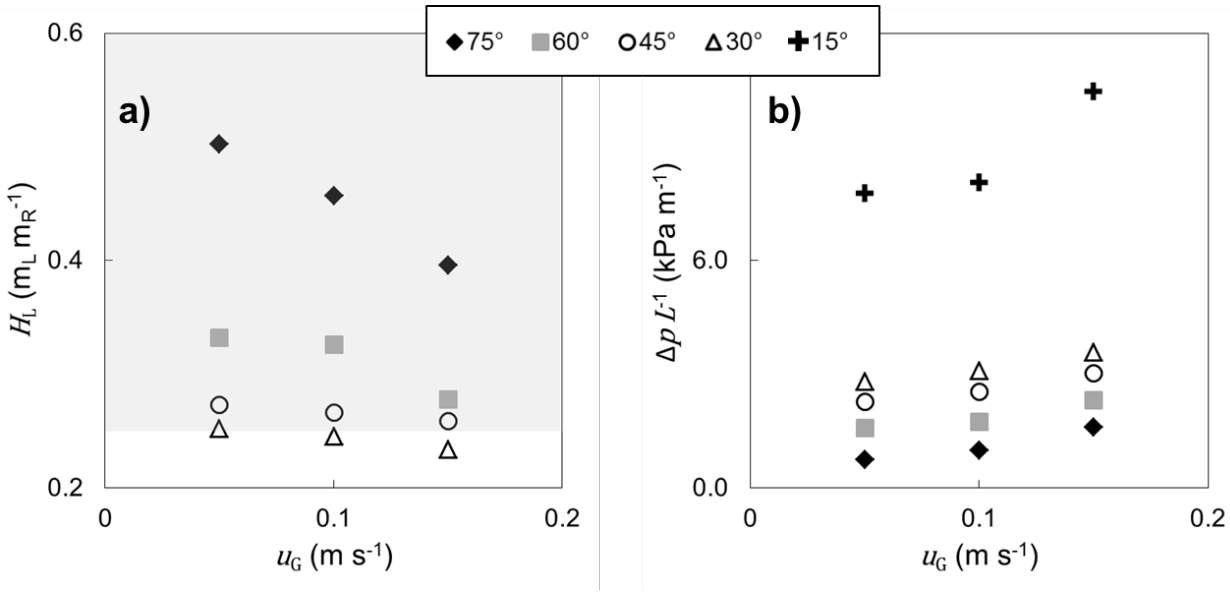

Figure 9: a) Liquid filling level H_L and b) specific pressure drop $\Delta p\, L^{-1}$ as a function of the superficial gas velocity (D_T = 5 cm, d_P = 4.5 mm, n = 1 rpm, u_L = 0.01 m s^{-1}).

H_L decreases with increasing superficial gas velocity for all cases. The higher shear rate at the gas-liquid interface accelerates the liquid. This effect is very pronounced at the highest inclination angle as a result of the high interstitial phase velocity difference. Here, the axial bulk velocity of the liquid phase is comparably low as the liquid height is built up, while the remaining area available for the gas phase decreases, causing a higher interstitial gas velocity. Logically, the specific pressure drop increases with higher superficial gas velocity due to increasing gas-solid and gas-liquid interactions.

At the same time, the phase distinction for the stratified flow patterns remains stable without significant liquid entrainment towards the drained sections as shown in Figure 10.

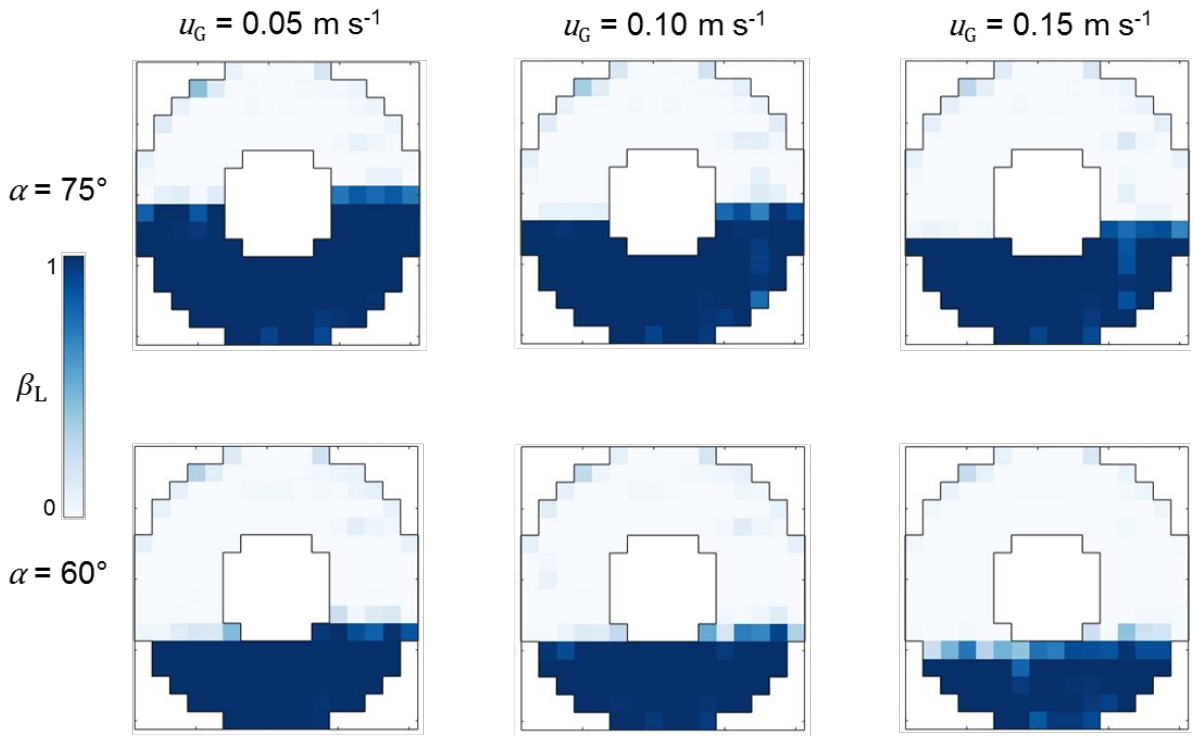

Figure 10: Effect of the superficial gas velocity on the gas-liquid distribution (D_T = 5 cm, d_P = 4.5 mm, n = 1 rpm, u_L = 0.01 m s^{-1}).

High superficial gas velocities in the IRR foster the gas-solid mass transfer, and in turn, the reaction rate for gas-limited reactions. Following this, the superficial gas velocity should be increased to reach saturation of the gaseous educts at the catalyst surfaces as long as stratification is maintained. On the other hand the gas-solid interactions should not exceed conditions at which particle pores start to dry out and depletion of liquid educt leads to a limitation of the reaction rate.

3.4 Effects of particle size and inner tube diameter

In fixed-bed reactors the particle diameter is decisive for liquid saturation, pressure drop and fluid-particle mass transfer. Thus, the effect of different spherical porous alumina particles on the hydrodynamics of the IRR is analysed for the

Configurations A and B. In Figure 11 H_L and $\Delta p\, L^{-1}$ are shown for different inclination angles.

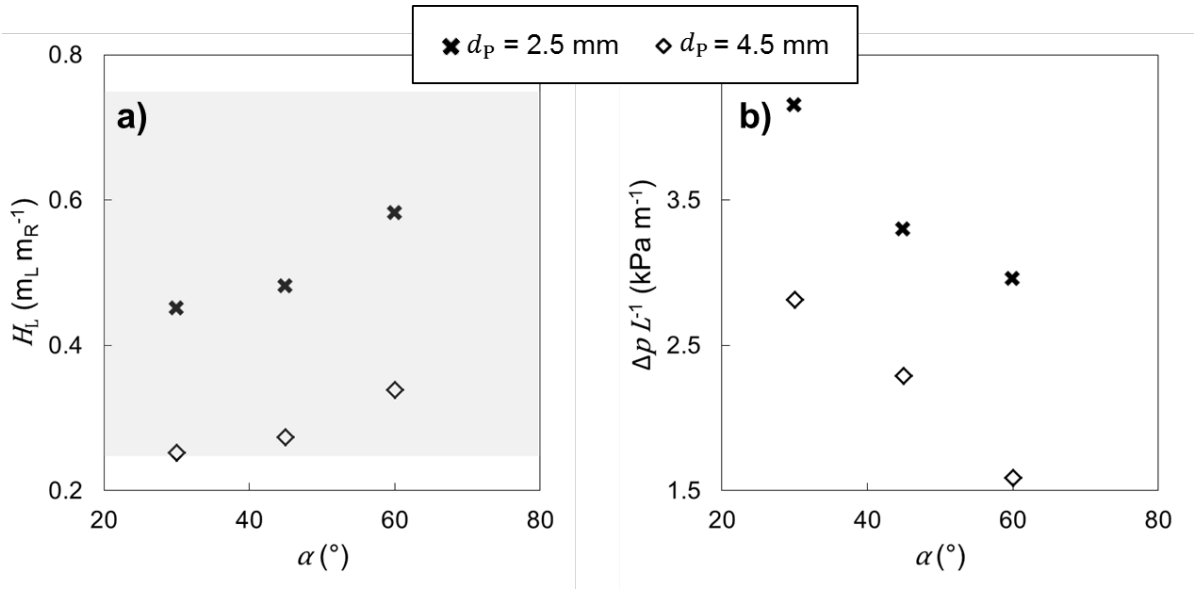

Figure 11: Comparison of a) liquid filling level H_L and b) specific pressure drop $\Delta p\, L^{-1}$ for Configurations A (d_P = 4.5 mm) and B (d_P = 2.5 mm) depending on the inclination angle (n = 1 rpm, u_L = 0.01 m s^{-1}, u_G = 0.05 m s^{-1}, D_T = 5 cm)

Under the same operating conditions H_L is significantly higher for Configuration B compared to Configuration A regardless of the inclination angle. Here, the higher specific surface area of Configuration B causes significant higher fluid-solid interactions. Thus, the liquid velocity decreases and liquid accumulates. Moreover, the average porosity of Configuration B is lower as a result of the lower bulk porosity (see Table 2). Consequently, less void space is accessible for the fluids, which yields a higher displacement of the liquid in Configuration B. Accordingly, the pressure drop is significantly higher for Configuration B.

Furthermore, the cross-sectional gas-liquid patterns reveal a smaller process window for Configuration B. A significant entrainment of liquid is already observed at an inclination angle of $\alpha = 60°$ and a rotational velocity of $n = 10$ rpm for the small particle packing, while distinct stratification is obtained at the same operating conditions for the larger particles up to an inclination angle of $\alpha = 45°$(Figure 12). The

earlier transition to sickle and dispersed flow for Configuration B results from higher fluid-solid interactions caused by the smaller particles as explained above.

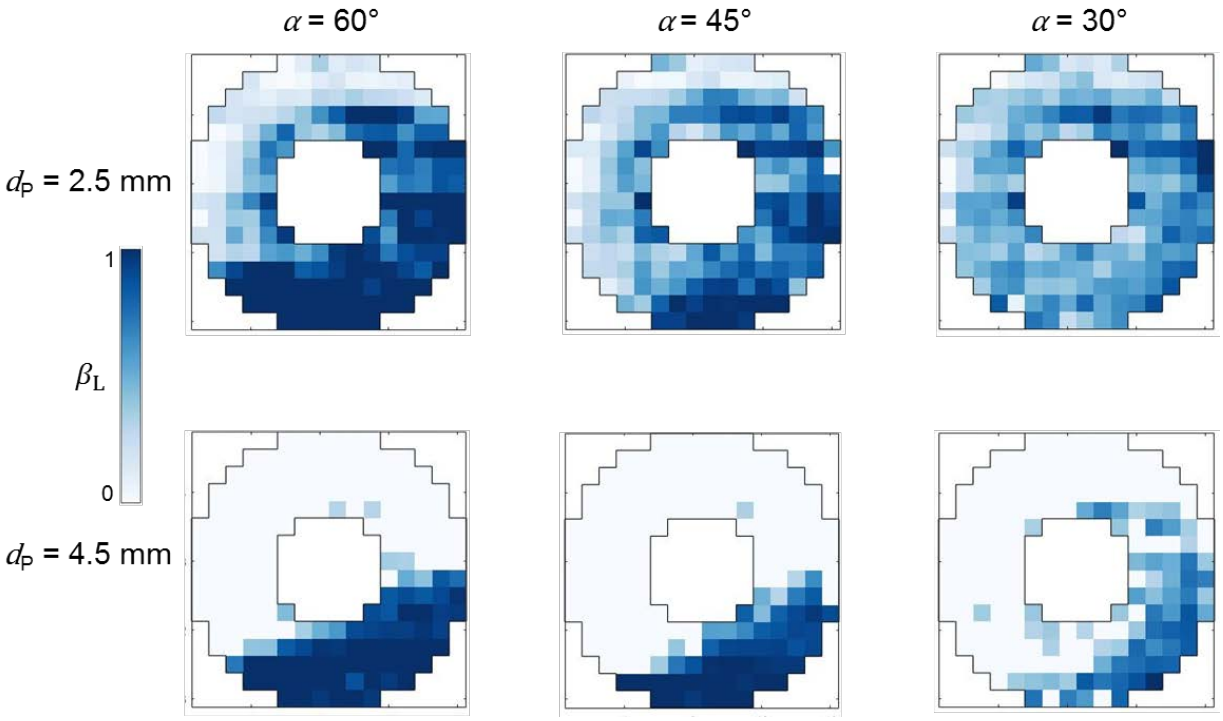

Figure 12: Effect of the particle diameter (lower row: Configuration A with d_P = 4.5 mm, upper row: Configuration B with d_P = 2.5 mm) on the gas-liquid distribution (D_T = 5 cm, n = 10 rpm, u_L = 0.01 m s^{-1}, u_G = 0.05 m s^{-1}).

A basic design parameter of the IRR is the inner tube diameter D_T, which defines the hydrodynamic process window. Obviously, the reduction of D_T narrows the hydrodynamic process window. Nevertheless, for reactions or process conditions with better performance at higher H_L (0.35 < H_L <0.7), smaller inner tubes might be of advantage since the absolute mass flow is higher (at same superficial fluid velocities), i.e. lower investment costs compared to designs with larger inner tube diameter. Figure 13 shows the effect of different inner tube diameters on H_L for different inclination angles.

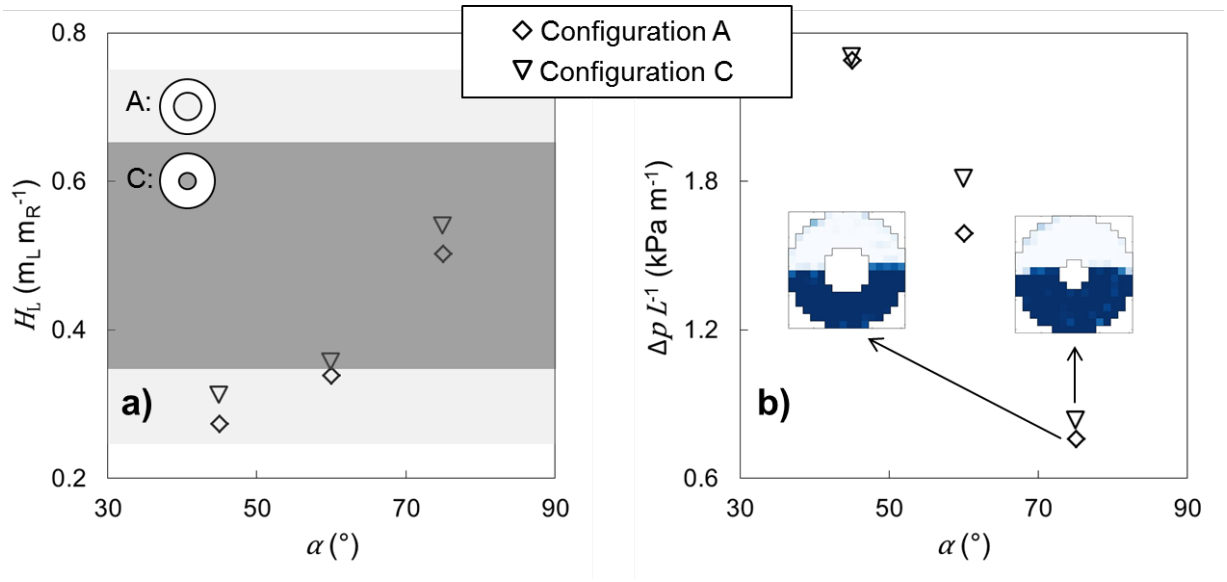

Figure 13: Effect of the inner tube diameter (Configuration A: D_T = 5 cm, Configuration C: D_T = 3 cm) on a) normalized liquid filling level H_L and b) specific pressure drop $\Delta p\ L^{-1}$ for different inclination angles (d_P = 4.5 mm, n = 1 rpm, u_L = 0.01 m s^{-1}, u_G = 0.05 m s^{-1}). The shaded areas denote the hydrodynamic process windows of Configuration A (bright grey) and C (dark grey), respectively.

Slightly smaller values for liquid filling level H_L and specific pressure drop are obtained for Configuration C with the smaller inner tube. The obtained differences are caused by the slightly lower porosity of Configuration C due to the smaller wall effect (see Table 2). The lower interstitial void space between the catalysts reduces the liquid residence time and increases the accumulation of the liquid.

All datasets analyzed in this Section are available in RODARE: 10.14278/rodare.204 [dataset] (Timaeus et al., 2019).

4 Conclusions

In this work, the hydrodynamic process windows, i.e. essential stratified flow pattern and range of the liquid filling level, and the specific pressure drop of an inclined rotating fixed-bed reactor with inner tube were studied for different design parameters. Besides, the wall effect of the additional inner tube on the porosity profile was characterized via gamma-ray CT. A capacitance wire-mesh sensor was used to visualize the liquid phase distribution in packings of porous alumina particles. Here,

the liquid filling level for the stratified flow patterns was derived averaging the local liquid saturations at the 176 crossing points.

Only minor effects of the rotational velocity were obtained at stratified flow conditions, while superficial phase velocities and inclination angle were found to have crucial effects. Arbitrary positions of the gas-liquid interface are adjustable in the IRR to adapt the durations for the liquid-solid and gas-solid contact depending on the prevailing mass transfer limitation of the reaction system. While the installation of a smaller tube revealed no significant influence on the investigated hydrodynamic parameters, smaller particle diameters were found to significantly increase the liquid filling level and the specific pressure drop, respectively.

Reaction studies will be carried out in another study to quantify the intensification potential of the inclined rotating fixed-bed reactor with inner tube for the located process window. Additionally, the new hydrodynamic data obtained in this study will further help to develop and validate a numerical model for a CFD-based reactor design as a next step.

Acknowledgement

The authors are grateful to the German Research Foundation for financial support (DFG SCHU 2421/2-3)

Symbols used

a	[-]	geometry-related constant 1
A	[m]	normalized attenuation coefficient
b	[-]	geometry-related constant 2
C	[-]	fitting parameter 1, porosity correlation
d_P	[m]	particle diameter
D	[m]	diameter
Δe	[-]	deviation between experiment and correlation

470	g	[m s^{-2}]	gravitational accelaration
471	h	[m]	filling level
472	H	[-]	normalized filling level
473	L	[m]	axial length of reactor
474	n	[rpm]	rotational velocity
475	N	[-]	fitting parameter 2, porosity correlation
476	p	[Pa]	pressure
477	r	[m]	radial coordinate
478	R	[m]	radius
479	u	[m s^{-1}]	superficial velocity
480	V	[V]	voltage
481	z	[m]	axial coordinate
482			
483	**Greek symbols**		
484	α	[°]	inclination angle towards the gravity
485	β	[m^3 m^{-3}]	reduced saturation
486	$\Delta p\ L^{-1}$	[kPa m^{-1}]	specific pressure drop
487	ρ	[kg m^{-3}]	density
488	ε	[-]	relative permittivity
489	ε	[m_V^3 m_R^{-3}]	porosity
490	Φ	[°]	azimuthal coordinate
491			
492	**Sub- and Superscripts**		

a	azimuthal
ave	average
b	bulk
bed	packed bed with porous alumina spheres
G	gas
L	liquid
max	maximum
Meas	measured
min	minimum
O	outer tube
P	particle
R	reactor
T	inner tube
V	void
X	fluid contributors

Abbreviations

CT	gamma-ray computed tomography
IRR	inclined rotating fixed-bed reactor
STY	space-time yield
TBR	trickle-bed reactor
WMS	wire-mesh sensor

References

Banchero, M., Manna, L., Sicardi, S., Ferri, A., 2004, Experimental investigation of fast-mode liquid modulation in a trickle-bed reactor, Chem. Eng. Sci. 59, 4149 – 4154. https://doi.org/10.1016/j.ces.2004.03.048

Bieberle, A., Schubert, M., da Silva, M. J., Hampel, U., 2010, Measurement of liquid distributions in particle packings using wire-Mesh sensor versus transmission tomographic imaging, Ind. Chem. Res. 49, 9445 – 9453. https://doi.org/10.1021/ie100900g

Boelhouwer, J. G., Piepers, H. W., Drinkenburg, B. A. H., 2002a, Advantages of forced non-steady operated trickle-Bed reactors, Chem. Eng. Technol. 25, 647 – 650. https://doi.org/10.1002/1521-4125(200206)25:6<647::AID-CEAT647>3.0.CO;2-9

Boelhouwer, J. G., Piepers, H. W., Drinkenburg, A. A. H., 2002b, Liquid-induced pulsing flow in trickle-bed reactors, Chem. Eng. Sci. 57, 3387 – 3399. https://doi.org/10.1016/S0009-2509(02)00210-5

Castellari, A. T., Haure, P. M., 1995, Experimental study of the periodic operation of a trickle-bed reactor, AIChE 41, 1593 – 1597. https://doi.org/10.1002/aic.690410624

Cheng, P., Hsu, C. T., 1986, Fully-developed, forced convective flow through an annular packed-sphere bed with wall effects, Int. J. Heat Mass Tran. 29, 1843 – 1853. https://doi.org/10.1016/0017-9310(86)90003-7

Dietrich, W., Grünewald, M., Agar, D. W., 2005, Dynamic modelling of periodically wetted catalyst particles, Chem. Eng. Sci. 60, 6254 – 6261. https://doi.org/10.1016/j.ces.2005.03.054

Edouard, D., Lacroix, M., Pham, C., Mbodji, M., Pham-Huu, C., 2008, Experimental measurements and multiphase flow models in solid SiC foam beds, AIChE 54, 2823 – 2832. https://doi.org/10.1002/aic.11594

Gelhausen, M. G., Yang, S., Cegla, M., Agar, D. W., 2017, Cyclic mass transport phenomena in a novel reactor for gas–liquid–solid contacting, AIChE 63, 208 – 215. https://doi.org/10.1002/aic.15532

546 Haase, S., Murzin, D. Y., Salmi, T., 2016, Review on hydrodynamics and mass
547 transfer in minichannel wall reactors with gas–liquid Taylor flow, Chem. Eng.
548 Res. Des. 113, 304 – 329. https://doi.org/10.1016/j.cherd.2016.06.017

549 Härting, H. U., Lange, R., Larachi, F., Schubert, M., 2015, A novel inclined rotating
550 tubular fixed bed reactor concept for enhancement of reaction rates and
551 adjustment of flow regimes, Chem. Eng. J. 281, 931 – 944.
552 http://dx.doi.org/10.1016/j.cej.2015.06.092

553 Hunt, M. L., Tien, C. L., 1990, Non-Darcian flow, heat and mass transfer in catalytic
554 packed-bed reactors, Chem. Eng. Sci. 45, 55 – 63. https://doi.org/10.1016/0009-
555 2509(90)87080-C

556 Hunt, M. L., Tien, C. L., 1988, Non-darcian convection in cylindrical packed beds, J.
557 Heat Transfer 110, 378 – 384. https://doi.org/10.1115/1.3250495

558 Khadlikar, M. R., Al-Dahhan, M. H., Duduković, M. P., 1999, Parametric study of
559 unsteady-state flow modulation in trickle-bed reactors, Chem. Eng. Sci. 54, 2585
560 – 2595. https://doi.org/10.1016/S0009-2509(98)00426-6

561 Lange, R., Hanika, J., Stradiotto, D., Hudgins, R. R., Silveston, P. L., 1994,
562 Investigations of periodically operated trickle-bed reactors, Chem. Eng. Sci. 49,
563 5615 – 5621. https://doi.org/10.1016/0009-2509(94)00363-7

564 Mills, P. L., Duducović, M. P., 1980, Analysis of catalyst effectiveness in trickle-bed
565 reactors processing volatile or nonvolatile reactants, Chem. Eng. Sci. 35, 2267 –
566 2279. https://doi.org/10.1016/0009-2509(80)87004-7

567 Nigam, K. D. P., Larachi, F., 2005, Process intensification in trickle-bed reactors,
568 Chem. Eng. Sci. 60, 5880 – 5894. https://doi.org/10.1016/j.ces.2005.04.061

569 Nijhuis, T. A., Kreutzer, M. T., Romijn, A. C. J., Kapteijn, F., Moulijn, J. A., 2001,
570 Monolithic catalysts as efficient three-phase reactors, Chem. Eng. Sci. 56, 823 –
571 829. https://doi.org/10.1016/S0009-2509(00)00294-3

572 Prasser, H. M., Böttger, A., Zschau, J., 1998, A new electrode-mesh tomograph for
573 gas–liquid flows, Flow. Meas. Instrum. 9, 111 – 119.
574 https://doi.org/10.1016/S0955-5986(98)00015-6

Schubert, M., 2018, DE 10 2018 110 091.4.

da Silva, M. J., Schleicher, E., Hampel, U., 2007, Capacitance wire-mesh sensor for fast measurement of phase fraction distributions, Meas. Sci. Technol. 18, 2245 – 2251. https://doi.org/10.1088/0957-0233/18/7/059

Sodré, J. R., Parise, J. A. R., 1998, Fluid flow pressure drop through an annular packed bed of spheres with wall effects, Exp. Therm. Fluid Sci. 17, 265 – 275. https://doi.org/10.1016/S0894-1777(97)10022-X

Timaeus, R., Hampel, U., Schubert, M., 2019a, Heterogeneous modeling approach for gas-limited reactions in an inclined rotating fixed bed reactor, Chem. Ing. Tech. 91, 637 – 644. https://doi.org/10.1002/cite.201800183

Timaeus, R., Berger, R., Schleicher, E., Hampel, U., Schubert, M., 2019b, Liquid flow visualization in packed-bed multiphase reactors: wire-mesh sensor design and data analysis for rotating fixed beds, Chem. Ing. Tech. 91, 1 – 11. https://doi.org/10.1002/cite.201900117

Timaeus, R., Schleicher, E., Bieberle, A., Hampel, U., Schubert, M., 2019c, Hydrodynamic data of an advanced inclined rotating fixed-bed reactor, RODARE repository. https://doi.org/10.14278/rodare.204

du Toit, C. G., 2008, Radial variation in porosity in annular packed beds, Nucl. Eng. Des. 238, 3073 – 3079. https://doi.org/10.1016/j.nucengdes.2007.12.018

Utikar, R. P., Ranade, V., V., 2017, Intensifying multiphase reactions and reactors: strategies and examples, ACS Sustain. Chem. Eng. 5, 3607 – 3622. https://doi.org/10.1021/acssuschemeng.6b03017

Vortmeyer, D., Schuster, J., 1983, Evaluation of steady flow profiles in rectangular and circular packed beds by a variational method, Chem. Eng. Sci. 38, 1691 – 1699. https://doi.org/10.1016/0009-2509(83)85026-X

Wallenstein, M., Kind, M., Dietrich, B., 2014, Radial two-phase thermal conductivity and wall heat transfer coefficient, Int. J. Heat Mass Transf. 79, 486 – 495, http://dx.doi.org/10.1016/j.ijheatmasstransfer.2014.08.003

603 Zalucky, J., Wagner, M., Schubert, M., Lange, R., Hampel, U., 2017a,
604 Hydrodynamics of descending gas-liquid flows in solid foams: Liquid holdup,
605 multiphase pressure drop and radial dispersion, Chem. Eng. Sci. 168, 480 – 494.
606 http://dx.doi.org/10.1016/j.ces.2017.05.011

607 Zalucky, J., Schubert, M., Lange R., Hampel, U., 2017b, Dynamic liquid−solid mass
608 transfer in solid foam packed reactors at trickle and pulse flow, Ind. Eng. Chem.
609 Res. 56, 13190 – 13205. https://doi.org/10.1021/acs.iecr.7b01578